

10.3

Cardiac Image Processing

Joseph M. Reinhardt
University of Iowa

William E. Higgins
Penn State University

1	Introduction.....	1175
2	Coronary Artery Analysis	1176
2.1	Single-Plane Angiography • 2.2 Biplane Angiography and 3D Reconstruction • 2.3 X-ray CT Imaging • 2.4 Intravascular Ultrasound Imaging • 2.5 Virtual Angioscopy	
3	Analysis of Cardiac Mechanics and Shape	1183
3.1	Chamber Analysis • 3.2 Myocardial Wall Motion and Wall Mechanics	
4	Myocardial Blood Flow (Perfusion).....	1190
5	Electrocardiography	1190
6	Summary and View of the Future	1190
	Acknowledgments.....	1191
	References.....	1191

1 Introduction

Heart disease continues to be the leading cause of death. According to the Centers for Disease Control and Prevention, over 700,000 fatalities due to heart disease were reported in the United States alone in 2001. Imaging techniques have long been used for assessing and treating cardiac disease [1–3]. Among the imaging techniques employed are x-ray angiography, x-ray computed tomography (CT), ultrasonic imaging, magnetic resonance (MR) imaging, positron emission tomography (PET), single-photon emission tomography (SPECT), and electrocardiography. These options span most of the common radiation types and have their respective strengths for assessing various disease conditions. Chapter 10.2 further discusses some relevant image-formation techniques and references [1–3] give a general discussion on cardiac image-formation techniques.

The heart is an organ that is constantly in motion. It receives deoxygenated blood from the body's organs via the venous circulation system (veins). It sends out oxygenated blood to the body via the arterial circulation system (arteries). The heart itself receives some of this blood via the coronary arterial network. Disease arises when the blood supply to the heart is interrupted or when the mechanics of the cardiac cycle change.

The available cardiac-imaging modalities produce a wide range of image data types for disease assessment: 2D projection images, reconstructed 3D images, 2D slice images, true 3D images, time sequences of 2D and 3D images, and sequences of 2D interior-view (endoluminal) images. Each type of data introduces different processing issues. Fortunately, extensive effort has been made to devise computer-based techniques for managing this data and for extracting the useful information. This chapter focuses on techniques for processing cardiac images. Since a cardiac image is generally formed to diagnose a possible health problem, it is always essential that the physician have considerable control in managing the image data. Thus, visualization and manual data interaction play a major role in processing cardiac images. In general, the physician uses computer-based processing for guidance, not as the “final word.” The various techniques for processing cardiac images can be broken down into four main classes:

1. Examination of the coronary arteries to find narrowed (stenosed) arteries.
2. Study of the heart's mechanics and shape during the cardiac cycle.
3. Analysis of the temporal circulation of the blood through the heart.

4. Mapping of the electrical potentials on the heart's surfaces.

Subsequent sections of this chapter will focus on each of these four areas.

2 Coronary Artery Analysis

Perhaps the largest application of cardiac imaging is in the identification and localization of narrowed or blocked coronary arteries. Arteries become narrowed over time via a process known as coronary calcification ("hardening of the arteries"). If a major artery becomes completely blocked, this causes myocardial infarction ("heart attack"); the blood supply to the part of the heart provided by the blocked artery stops, resulting in tissue damage and, in many instances, death.

The region where an artery is narrowed or blocked is referred to as a stenosis. In the discussion to follow, the arteries will often be referred to as vessels. The inside of an artery is known as the lumen. The arterial network to the heart is often referred to as the coronary arterial tree. The major imaging modalities for examining the coronary arteries are x-ray angiography, CT imaging, intravascular ultrasound, and virtual angioscopy. MR angiography, similar to x-ray angiography, is also possible. Digital image-processing techniques exist for all of these image types. As described below, the primary aim of these methods is to provide human-independent aids for assessing the condition of the coronary arteries.

2.1 Single-Plane Angiography

Historically, angiography imaging has been the standard for cardiovascular imaging. In angiography, a catheter is inserted into the body and positioned within the anatomic region under study. A contrast agent is injected through the catheter, and x-ray projection imaging is used to track the flow of contrast through the anatomy. An immediate problem with this imaging set-up is that 3D anatomic information is mapped onto a 2D plane. This results in information loss, structural overlap, and ambiguity.

Images may be obtained in a single plane or in two orthogonal planes (biplane angiography). Such images are referred to as angiograms. For coronary angiography, the contrast is used to highlight the coronary arteries. Figure 1 depicts a typical 2D angiogram containing a stenosed artery.

The size of pixels in a digitized angiogram is on the order of 0.1 mm, permitting visualization of arteries around 1.0 mm in diameter. Sometimes separate angiograms can be collected before and after the contrast agent is introduced. Then, the no-contrast image is subtracted from the contrast-enhanced image to give an image that nominally contains only the

enhanced coronary arteries. This procedure is referred to as digital subtraction angiography (DSA) [1, 2, 5].

For an x-ray coronary angiogram f , the value $f(x, y)$ represents the line integral of x-ray attenuation values of tissues situated along a ray L originating at the x-ray source and passing through the body to strike a detector at location (x, y) :

$$f(x, y) = \int_{L_{x,y}} \mu(x, y, z) dz$$

where L represents the ray (direction of x-ray) emanating from point (x, y) and $\mu(x, y, z)$ represents the attenuation coefficient of tissues. Encountered tissues can include muscle, fat, bone, blood, and contrast-enhanced blood. The value $f(x, y)$ tends to be darkest for rays passing through the contrast-enhanced arteries, since the contrast agent is radio-dense (fully absorbs transmitted x-rays). Thus, the arteries of interest tend to appear dark in angiograms. The main image-processing problem is to locate the dark, narrow, branching structures—presumably this is the coronary arterial tree—and estimate the diameter or cross-sectional area along the extent of each identified branch. A stenosis is characterized by a local minimum in vessel diameter or cross-sectional area.

Pappas proposed a complete mathematic model for structures contained in a 2D angiogram [6]. In this model, a contrast-enhanced vessel is represented as a generalized cylinder having elliptical cross-section; the 2D projection of this representation can be captured by a function determined

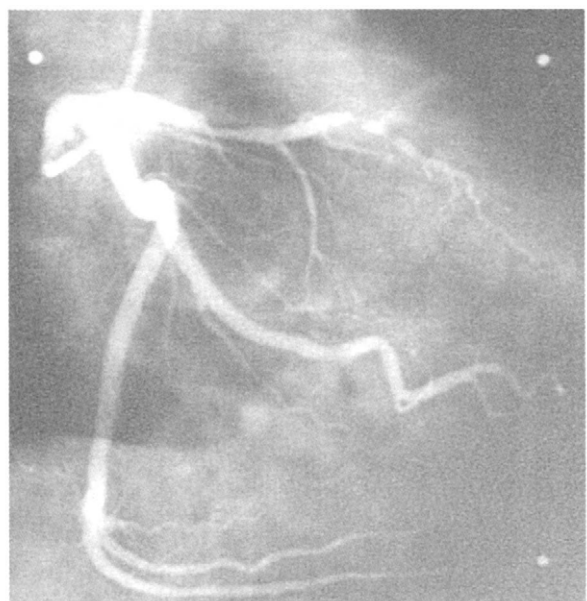


FIGURE 1 A typical 2D angiogram. Image intensity is inverted to show the arteries as bright structures. The artery running horizontally near the top clearly shows a stenosis. From [4].

by two parameters. The background tissues (muscle, fat, etc.) are modeled by a low-order slowly-varying polynomial, since such structures presumably arise from much bigger, and hence, slowly-varying functions. During the imaging process, unavoidable blurring occurs in the final image; this introduces another factor. Finally, a small noise component arises from digitization and attenuation artifacts. Thus, a point $f(x, y)$ on an angiogram can be modeled as

$$f(x, y) = \int_{L_{x,y}} (((v(x, y, z) + b(x, y, z)) * g(z)) + n(z)) dz \quad (1)$$

where $v(x, y, z)$ represents a contrast-enhanced vessel, $b(x, y, z)$ represents the background, $g(z)$ is a Gaussian-smoothing function to account for image blurring, and $n(z)$ denotes the noise component. Pappas proposed a method where parameters of this model can be estimated using an iterative maximum-likelihood (ML) estimation technique. The procedure enables reasonable extraction of major arteries. Most importantly, it also provides estimates of vessel cross-sectional area profiles (a function showing the cross-sectional area measurement along the extent of a vessel). This permits identification of vessel stenoses.

Fleagle et al. proposed a fundamentally different approach for locating the coronary arteries and estimating vessel-diameter profiles [7]. Their study uses processing elements common to many other proposed approaches and contains many tests on real image data.

The first step of their approach requires a trained human observer to manually identify the centerline (central axis) of each artery of interest. The human uses a computer mouse to identify a few points that visually appear to approximately pass through the center of the vessel. Such manual intervention is common in many medical imaging procedures. These identified centerline points are then smoothed, using an averaging filter to give a complete centerline estimate. This step need not take more than 10 seconds per vessel. Next, two standard edge-detection operators—a Sobel operator and a Marr-Hildreth operator—are applied. A weighted sum of these output edge images is then computed. The composite edge image is then resampled along lines perpendicular to the centerline, at each point along the centerline. This produces a 2D profile where the horizontal coordinate equals distance along the centerline and the vertical data corresponds to the composite edge data. In effect, this resampled data represents a “straightened out” form of the artery. Next, this warped edge image is filtered, to reduce the effect of vessel border blurring, and a graph-search technique is applied to locate vessel borders. Finally, the detected borders are mapped back into the original space of the angiogram $f(x, y)$ to give the final vessel borders and diameters.

Sun et al. proposed a method especially suited for the insufficient resolution often inherent in digitized angiograms [8].

A human user first manually identifies the beginning and ending points of a vessel of interest. An adaptive tracking algorithm is then applied to identify the vessel’s centerline. This centerline then serves as the axis traveled by a direction-sensitive low-pass filter. For each point along the centerline, angiographic data perpendicular to the centerline is retrieved and filtered. This new data is then filtered by a low-pass differentiator to identify vessel walls (outer borders). The differentiator acts as an edge detector. Figure 2 gives a typical output from this technique.

As an alternative to border-finding techniques, Klein et al. proposed a technique based on active contour analysis [9]. In their approach two direction-sensitive Gabor filters are applied to the original angiogram. These filtered images are then combined to form a composite energy-field image. The human operator then manually identifies several control points on this image to seed the contour finding process. Two B-spline curves, corresponding to the vessel borders, are then computed using an iterative dynamic-programming procedure. Figure 3 gives an example from the procedure.

2.2 Biplane Angiography and 3D Reconstruction

Modern angiography generally uses views from more than one image plane of data. Biplane angiography involves generating two 2D angiograms at different viewing angles. Since the major coronary arteries are contrast enhanced, they can be readily identified and matched in the two given angiograms. This admits the possibility of 3D reconstruction of the arterial tree. 3D views provide many advantages over single 2D views: (1) they provide unambiguous positional information, which is useful for catheter insertion and surgical procedures, (2) they enable true vessel segment length and cross-sectional area calculations, and (3) they are useful for monitoring the absolute motion of the myocardium. Biplane angiography is essentially a form of stereo imaging, but the term “biplane” has evolved in the medical community. Many computer-based approaches have been proposed for 3D reconstruction of the arterial tree from a set of biplane angiograms [4, 5, 10, 11].

Parker et al. proposed a procedure where the user first manually identified the axes of the arterial tree in each given angiogram [10]. Next, a dynamic search, employing vessel edge information, improves the manually identified axes. A least-squares-based point-matching algorithm then correlates points from the two skeletons to build the final 3D reconstructed tree. The point-matching algorithm takes into account manually identified key points, the sparseness of the 3D data, and the known geometry between the two given angiograms.

Kitamura et al. proposed a two-stage 3D reconstruction technique [5]. First, the skeleton (central axes) and artery boundaries are computed for each 2D angiogram. Next,

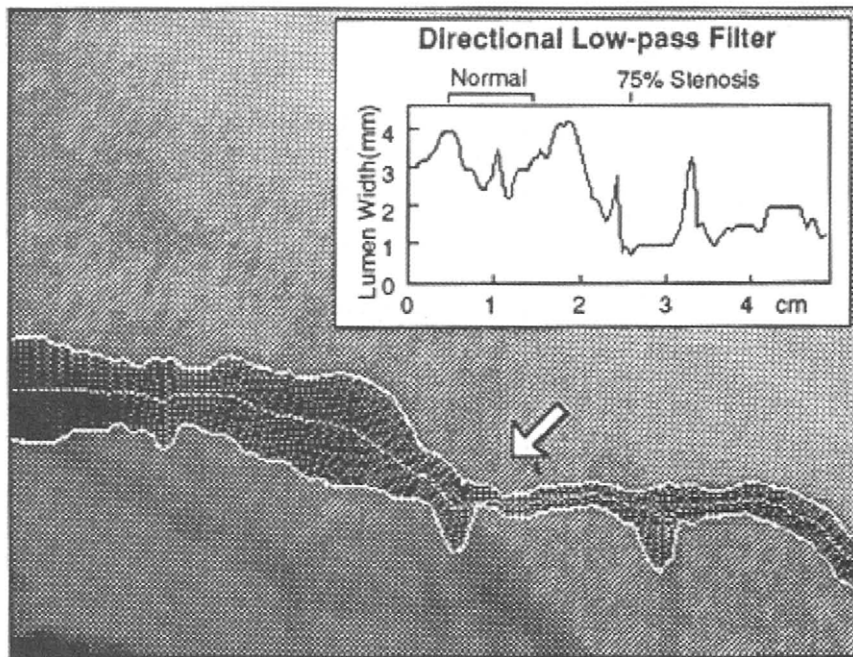


FIGURE 2 Example of an extracted artery and associated vessel-diameter (lumen-width) profile. The arrow points to the stenosis. From [8].

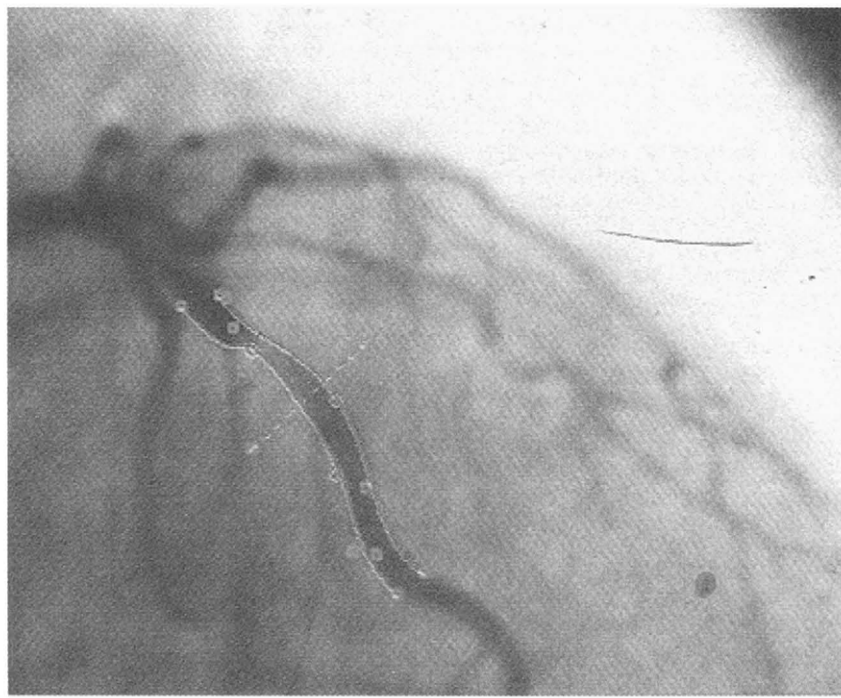


FIGURE 3 Result of active-contour analysis applied to a selected artery in a typical 2D angiogram. The green points are the manually identified control points. The red lines are the computed vessel wall borders. From [9]. (See color insert.)

a correspondence technique is applied to build a 3D reconstructed artery model and skeleton.

Stage 1 employs the same generalized cylinder model (1) as Pappas [6]. Figure 4 shows a portion of this

model and its relationship to each of the two known angiograms. Kitamura et al. allow the user to manually set parameters for all artery end points. Thus, all preidentified parts of the arterial tree are estimated. A nonlinear

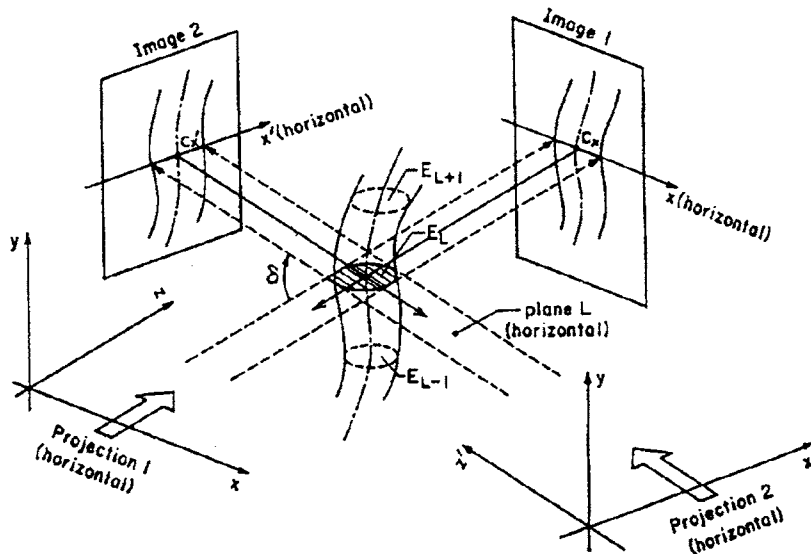


FIGURE 4 Geometry for reconstructing the 3D arterial tree from two biplane images. The artery is modeled as a generalized cylinder having elliptical 2D cross-sections. These cross-sections project as weighted line segments onto the two known 2D angiograms (Images 1 and 2). From [5].

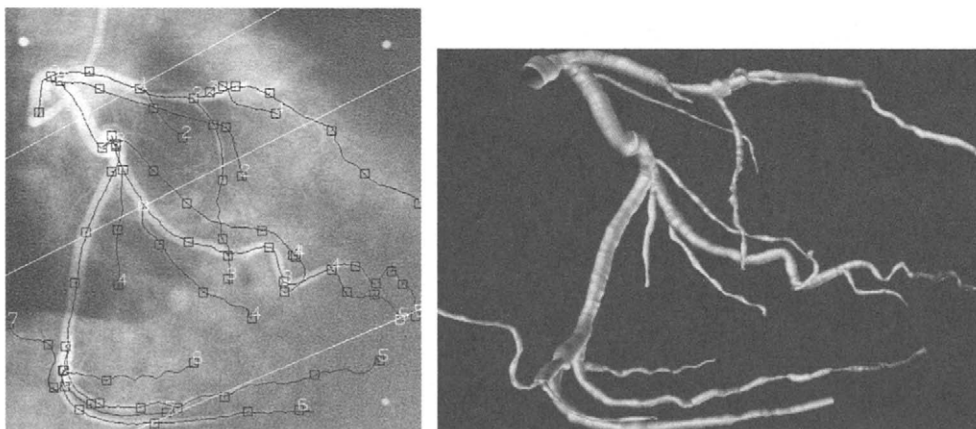


FIGURE 5 Extracted 3D tree using the method of Wahle et al. Left figure shows the angiogram with superimposed tree (angiogram is the same as Figure 1). Right figure shows the reconstructed rendered 3D tree. From [4].

least-squares technique is used to estimate the model parameters. A few arteries can be situated parallel to the transmitted x-rays; these ill-defined portions of branches must be manually preidentified. Stage 2 reconstruction requires the user to manually identify bifurcation points (where a mother artery forms two smaller daughter branches) and stenotic points (where a stenosis occurs). These identified points then enable an automatic correspondence calculation of all skeleton points for the two reconstructed trees. This is done by backprojecting the points from the two trees into 3D space, as depicted in Fig. 4. Since the structure of the 3D tree is known from the manually identified points, the resulting correspondence is straightforward. The final output is a 3D reconstructed tree and associated cross-sectional areas.

Wahle et al. [4] used their 3D reconstruction system not only for visualization and local measurements, but also to

assess diffuse atherosclerosis. Since plaque itself is not angiographically visible, an indirect quantification was performed based on the vessel lumen over the fully reconstructed 3D vessel hierarchy. Figure 5 shows typical reconstruction results from the system of Wahle et al.

Note that the general anatomy of the coronary arterial tree is well known, even though it varies between patients. Also, the imaging geometry is known. This admits the possibility of using a knowledge-based system for reconstructing the 3D arterial tree. Recently, Liu and Sun proposed such a method that is fully automatic [11].

2.3 X-ray CT Imaging

Recently, ultrafast high-resolution x-ray CT has emerged as a true 3D cardiac imaging technique. CT can give detailed

information on the 3D geometry and function of the heart. Because of the heart motion during the cardiac cycle, high-speed scanning combined with ECG-gated image acquisition is required to obtain high-resolution images. Over the past twenty years, cardiac imaging has been performed on x-ray CT machines, such as the experimental dynamic spatial reconstructor (DSR) [12, 13], electron beam CT (EBCT) scanners [14], spiral (helical) CT scanners [15, 16], the modern multi-detector helical CT (MDCT) scanners [14], and x-ray micro-tomography (micro-CT) scanners [16, 17]. CT can provide a stack of 2D cross-sectional images to form a high-resolution 3D image. Thus, true 3D anatomic information is possible in a CT image, without the 2D projection artifacts of angiograms that cause structural ambiguities.

Once again, to image the coronary arteries, a contrast agent generally must be injected into the patient prior to scanning. Fortunately, the contrast can be injected intravenously, requiring significantly less invasion. Such an image is referred to as a 3D coronary angiogram. An early effort toward 3D coronary angiographic analysis, drawing on data from the DSR, can be found in [13]. The EBCT scanner has also received attention for use as an early screening device for coronary artery disease [14]. Multi-slice CT angiography, which uses an MDCT scanner, is an emerging technique [14, 17]. MDCT can serve as a complement or possibly replace the invasive procedure known as cardiac catheterization. It can also help assess plaque content, stenoses, myocardial viability, and atherosclerosis.

Current state-of-the-art micro-CT scanners give voxel resolution on the order of 0.001 mm (10 μm) [18, 19]. Micro-CT scanners are being used in the burgeoning field of small-animal imaging. Micro-CT images permit the tracking of anatomic changes in genetically engineered mice to determine the long-term impact of various genes on disease states. In addition, high-resolution micro-CT scanners enable the imaging of the microvasculature. This has spurred researchers to consider the complete analysis and description of a vascular tree [20]. Figure 6 gives a composite view of a complete system devised for this problem [19].

To use this system, three major steps are performed. First, automated image processing is performed to extract a raw 3D arterial tree. Next, potential defects in the arterial tree are located, and semi-automatic techniques are performed to correct the tree. Finally, quantitative analysis is performed to give a complete description of the tree. More detail appears below.

The first processing step uses automatic, 3D, digital image processing steps. The raw 3D micro-CT image I undergoes 3D nonlinear filtering to reduce image noise and sharpen the thin, bright arteries. Next, a 3D symmetric region-growing algorithm, which is invariant to the starting root of the tree, produces a segmented vascular tree I_S . Cavity filling and other shape-based image-processing operations, based on 3D mathematic morphology, are next applied to clean up

the raw segmentation I_S . (Chapter 2.2 discusses mathematic morphology.) Next, a triangular mesh, defined to the sub-voxel level, is created for the tree; the marching cubes algorithm is applied to the following gray-scale mask image IM to generate the mesh:

$$IM = (I_S \oplus B - I_S \ominus B) \times (I - I_{TH})$$

where B is a $3 \times 3 \times 3$ structuring element, \oplus and \ominus are morphologic dilation and erosion, and I_{TH} is a thresholded image created during symmetric region growing. Finally, using concepts from differential geometry, a precise description of the arterial tree's central axes are derived from the fine surface mesh.

During the second processing step, the user draws upon a sophisticated graphical user interface system to interact with extracted tree and central axes. The system provides a simple enumeration of potential defects, such as implausible loops, possible broken branches, overly close branch/bifurcation points, and trifurcations. With the assistance of a series of visualization tools, such as 3D surface rendering, sliding thin slabs, 2D projections, a map of the tree's graph, and 2D slice images, the user can see the data associated with each defect. Semi-automatic editing tools can be invoked to break loops, repair broken branches, and perform other tree corrections. After the tree is deemed satisfactory, the third automated processing step derives a complete quantitative description of the tree. See Fig. 6 for an example. In the figure, the quantitative data are as follows: "GenID" = generation index, "NumBr" = total number of branches in given generation, "AvgBrLen" = average length of a branch (mm), "AvgCSA" = average cross-sectional area for a branch (mm^2), "AvgSurf" average surface area of a branch (mm^2), "AvgVol" = average volume of a branch (mm^3) [18].

As shown in this example and in Section 2.4, 3D imaging applications routinely need visualization tools to give adequate means for assessing the image data beyond simple 2D image planes.

2.3.1 Magnetic Resonance Imaging

Magnetic resonance (MR) imaging uses RF magnetic fields to construct tomographic images based on the principle of nuclear magnetic resonance (NMR) [21]. The pixel values in MR images are a function of the chemical configuration of the tissue under study. For most imaging protocols the pixel values are proportional to the density of hydrogen nuclei within a region of interest, although new imaging techniques are being developed to measure blood flow and other physiologic parameters. Diagnostic MR imaging uses non-ionizing radiation, so exams can be repeated without the dangers associated with cumulative radiation exposure. Because the magnetic fields are electrically controlled, MR imaging is

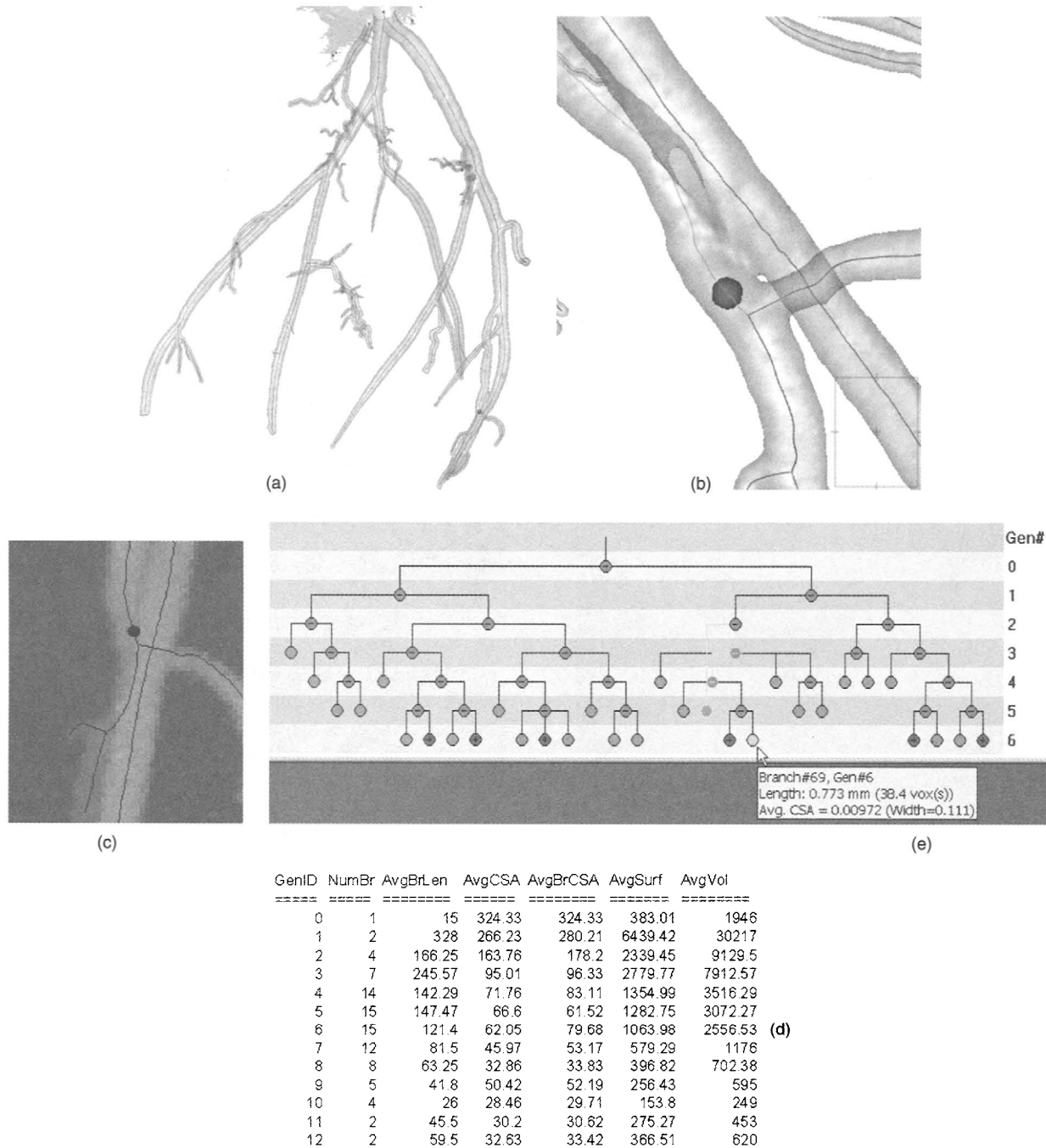


FIGURE 6 Composite view of system for analyzing a 3D arterial tree [19]. (a) Surface-rendered version of the extracted 3D arterial tree; a tree defect is marked by a ball; in all views the lines denote the tree central axes. (b) Local surface rendering of tree about the selected defect. (c) Local depth-weighted slab of original 3D gray-scale data about defect. (d) Quantitative description of final tree [18]. (e) Graph of corrected tree; nodes signify branch points; circles with plusses signify graph nodes that can be expanded further; a node (branch) is selected to show its local quantitative description. (See color insert.)

capable of gathering planar images at arbitrary orientations. MR imaging is commonly used to study the coronary arteries [22], see Fig. 7 for an MR image example showing the heart muscle and the right coronary artery.

2.4 Intravascular Ultrasound Imaging

Standard coronary angiography does not give reliable information on the cross-sectional structure of arteries. This makes it difficult to accurately assess the build up of plaque along

the artery walls. Intravascular ultrasound (IVUS) imaging has emerged as a complementary technique for providing such cross-sectional data [23]. To perform IVUS, a catheter equipped with an ultrasonic transducer is inserted into a vessel of interest. As the catheter is maneuvered through the vessel, real-time cross-sectional images are generated along the vessel's extent. Example angiographic and IVUS views of the same artery segment are shown in Fig. 8. IVUS, however, does not provide positional information for the device. But



FIGURE 7 MR image showing heart muscle, blood-filled cardiac chambers, and the right coronary artery. (Figure courtesy of Dr. Daniel Thedens, University of Iowa.)

when IVUS is used in conjunction with biplane angiography, precise positional information can be computed. Thus, 3D geometric descriptions, including surface reconstructions and detailed local cross-sectional information can be calculated [23], and these reconstructions can be used in applications such as wall plaque characterization, hemodynamics, and vessel mechanical analysis [23]. The reconstructed geometry can be presented using sophisticated viewing tools drawing upon the virtual reality modeling language (VRML). See Fig. 9 for an example.

To produce this view, standard biplane analysis, similar to that described in Section 2.2, must first be performed on a given pair of biplane angiograms. Next, the 3D position of the IVUS probe, as given by its spatial location and rotation, must be computed from the given sequence of IVUS cross-sectional images. This positional information can then be easily correlated to the biplane information.

2.5 Virtual Angioscopy

Virtual endoscopy has emerged as a popular method for visualizing and evaluating anatomic structures in high-resolution 3D medical images [25]. In virtual endoscopy, the user peers inside hollow organs noninvasively using a given 3D image as the “virtual environment.” The computer acts as a “virtual endoscope.” With virtual endoscopy, the physician can examine the interiors of organs with impunity. The physician can also use virtual endoscopy to plan or “rehearse” later live invasive procedures. The first such virtual-endoscopy views, often referred as endoluminal renderings, were generated in the early 1980s when 3D medical imaging modalities were first proposed. Figure 12, discussed in the next section, shows such renderings

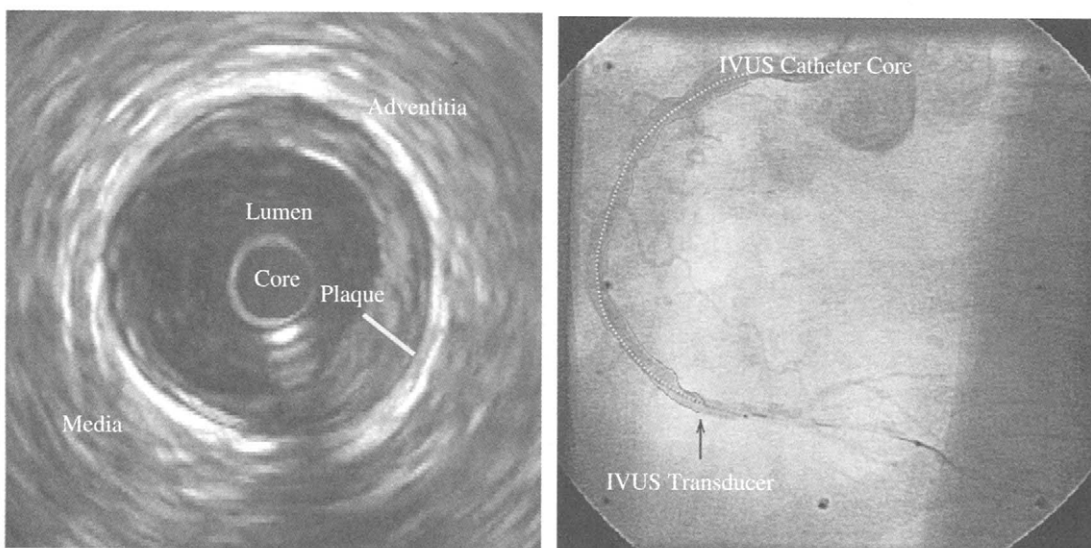


FIGURE 8 Angiographic and IVUS views of the coronary arteries. Right view is a 2D angiogram; arrow indicates location of the IVUS transducer. Left view shows corresponding cross-sectional IVUS frame of the arterial lumen. (See color insert.) (Figure courtesy of Dr. Andreas Wahle, University of Iowa.)

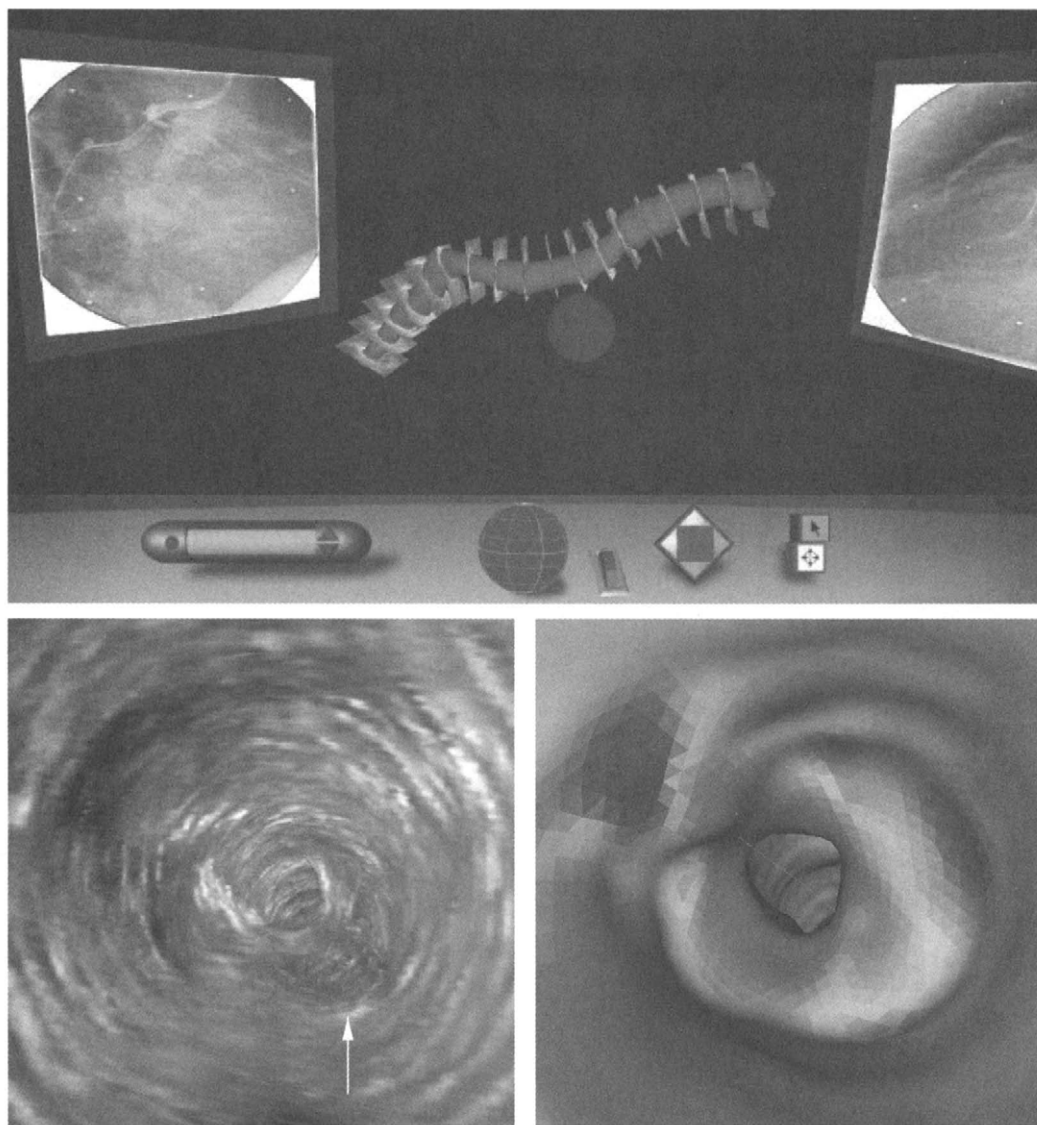


FIGURE 9 Views from a VRML-based angiographic-IVUS fusion system. Top shows VRML display and navigation system. Bottom view depicts a 3D virtual angioscopy view. The system of [19] also has the capability of depicting endoluminal renderings of arteries. From [24]. (See color insert.)

inside the heart chambers. When this field is specialized to the arteries, it is referred to as virtual angioscopy [25]. Figure 9 depicts a virtual angioscopy view. The system of [19] also has the capability of depicting endoluminal renderings of arteries.

3 Analysis of Cardiac Mechanics and Shape

Imaging can be used to make a clinically-meaningful assessment of heart structure and function. The human heart consists of four chambers separated by four valves. The right atrium receives deoxygenated blood from the

venous circulation and delivers it to the right ventricle. The right ventricle is a low pressure pump that moves the blood through the pulmonary artery into the lungs for gas exchange. The left atrium receives the oxygenated blood from the lungs and empties it into the left ventricle (LV). The LV is a high-pressure pump that distributes the oxygenated blood to the rest of the body. The heart muscle, called the myocardium, receives blood via the coronary arteries. During the diastolic phase of the heart cycle, the LV chamber fills with blood from the left atrium. At the end of the diastolic phase (end diastole) the LV chamber is at its maximum volume. During the systolic phase of the heart cycle, the LV chamber pumps blood to the systemic circulation. At the end of the systole phase (end systole), the LV chamber is at

its minimum volume. The cycle of diastole–systole repeats for each cardiac cycle.

Cardiac imaging can be used to qualitatively assess heart morphology, for example, by checking for a four-chambered heart with properly functioning heart valves. More quantitatively, parameters such as chamber volumes and myocardial muscle mass can be estimated from either 2D or 3D imaging modalities. If 3D images are available, it is possible to construct a 3D surface model of the inner and outer myocardium walls. If 3D images are available at multiple time points (a 4D image sequence), the 3D model can be animated to show wall motion and estimate wall thickening, velocity, and myocardial strain.

From an image engineering perspective, cardiac imaging provides a number of unique challenges. Since the heart is a dynamic organ that dramatically changes size and shape across the cardiac cycle (about 1 second), image acquisition times must be short or the cardiac structures will be blurred due to the heart motion. Good spatial resolution is required to accurately image the complex heart anatomy. Adjacent structures, including the chest wall, ribs, and lungs, all contribute to the difficulties associated with obtaining high quality cardiac images. A variety of image processing techniques, ranging from simple edge detection to sophisticated 3D shape models, have been developed for cardiac image analysis. Once the cardiac anatomy has been segmented in the image data, measurements such as heart chamber volume, ejection fraction, and muscle mass can be computed.

3.1 Chamber Analysis

The LV chamber is the high-pressure heart pump that moves oxygenated blood from the heart to other parts of the body. Assessment of LV geometry and function can provide information on overall cardiac health. Many cardiac image acquisition protocols and image analysis techniques have been developed specifically for imaging the LV chamber to estimate chamber volume. There are two specific points in

the cardiac cycle that are of particular interest: the end of the LV filling phase (end diastole), when the LV chamber is a maximum volume; and the end of the LV pumping phase (end systole), when the LV chamber is at minimum volume. Let V_{ES} and V_{ED} represent the end systolic and end diastolic chamber volumes. Then the total cardiac stroke volume $SV = V_{ED} - V_{ES}$, and the cardiac ejection fraction is $EF = SV/V_{ED}$. Both of these parameters can be used as indices of cardiac efficiency [26].

3.1.1 Angiography

Both single and biplane angiography can be used to study the heart chambers [2, 26]. For this analysis, sometimes called ventriculography, the imaging planes are typically oriented so that one image is acquired on a coronal projection (called the anterior–posterior, or A–P plane), and the other image is acquired on a sagittal projection (called the lateral, or LAT plane). A radio-opaque liquid is injected into the LV chamber to increase contrast between the LV chamber and surrounding myocardium. Images may be acquired at a single time point (e.g., end diastole or end systole), or a sequence of images can be acquired over time showing the changing geometry of the chamber across the entire heart cycle (cineangiography). An angiogram showing the contrast-enhanced LV chamber is shown in Fig. 10.

Once the projection images have been obtained, the boundary between the LV chamber and myocardium must be identified. The LV boundary can be manually traced using a computer mouse or trackball, and for single plane or biplane images acquired at only a small number of time points, this manual processing may be acceptable. However, for routine clinical use and in the case of cineangiography, manual analysis is prohibitively time-consuming. Computer-assisted processing can reduce the time required to analyze the data, and can eliminate human error and variability.

Automatic processing can be technically challenging because the LV chamber will be overlapped by nearby structures

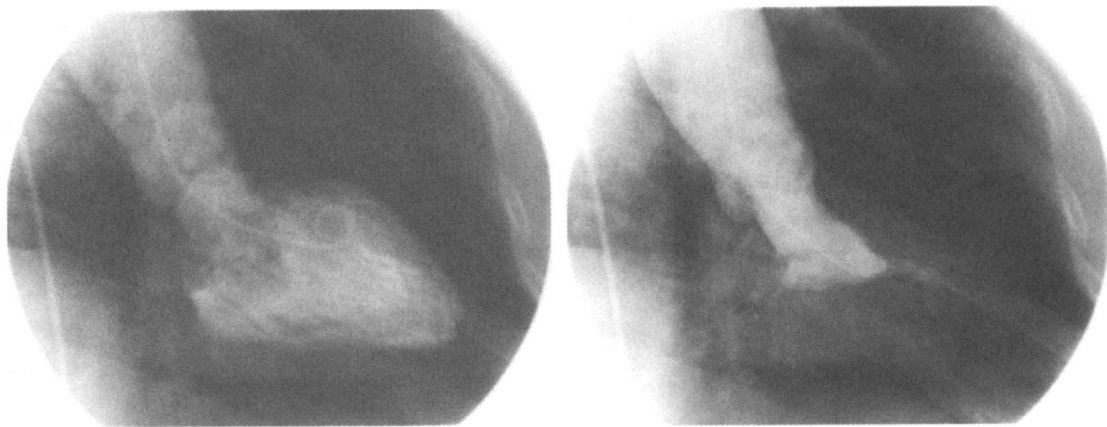


FIGURE 10 Angiographic images showing contrast-enhanced LV chamber. Left: End diastole. Right: End systole.
(Figure courtesy of the Adult Cardiac Catheterization Laboratory, University of Iowa.)



FIGURE 11 CT cross-sectional images of human thorax obtained using an electron beam CT scanner. Images show heart (oval-shaped gray region near center of images, with several bright ovals inside), lungs (dark regions on either side of heart), and vertebrae (bright regions at top middle). The heart region contains the myocardium (medium gray) and contrast-enhanced heart chambers (bright gray). (Images provided by Dr. Eric A. Hoffman, University of Iowa.)

(ribs, vessels, catheter, etc.) in the projection image. Some of this overlap problem can be addressed by using DSA. With DSA, a reference image (or image sequence) is acquired just prior to contrast injection. This reference can be digitally subtracted from the contrast-enhanced image to remove the background and overlapping adjacent structures. Care must be taken to gather both the reference image and contrast-enhanced image at exactly the same point in the cardiac and respiratory cycle [2]. Other challenges to automatic LV border detection include variations in the image intensity in the chamber due to inhomogeneous mixing of the contrast material, geometric distortions and nonlinearities in the imaging system, and random image acquisition noise [2].

Automatic and semi-automatic LV border detection methods typically identify the border as the local maximum of the image intensity gradient. Semi-automatic approaches rely on the operator to identify a starting pixel on the LV border, automatic methods may try to detect the starting location based on the image gradient. In either case, the border is tracked around the LV by computing the image gradient magnitude and direction. Constraints are used to construct a contour that approximately follows the gradient maximum around the border and encloses the LV with a closed, smooth curve [2].

Once the LV boundary has been identified, measurements can be made to assess heart function. The first step in making these measurements is to estimate the LV chamber volume from the boundaries identified on the projection images. Methods for computing chamber volume assume a 3D ellipsoidal chamber shape and require estimates of the minor and major axes of the ellipsoid from the projection images [26]. For single plane angiography, the ellipsoid is assumed to be rotationally symmetric about the long axis [2, 26].

3.1.2 Computed Tomography

X-ray CT imaging can also be used for heart chamber analysis. CT imaging is able to take advantage of injected contrast agents to better delineate the interface between the myocardium and the chamber. An example cardiac CT image with a contrast-enhanced LV chamber is shown in Fig. 11.

The cardiac chambers can be segmented by identifying the chamber boundaries on 2D CT slices, or more specialized 3D processing can be used. Once the chamber boundaries have been identified, the total chamber volume can be obtained by integrating over all the 2D cross-sectional areas across slices and scaling by the CT slice thickness. Because both the inner (endocardial) and outer (epicardial) borders of the myocardium can be identified on the CT images, parameters such as myocardial wall thickness and myocardial muscle volume can be computed [26].

Much of the early cardiac CT image analysis was performed manually. Manual image analysis requires that a skilled operator trace region boundaries on 2D slices projected on a computer screen. This processing is extremely time-consuming and prone to human error and variability. A number of methods for automatic and semi-automatic LV chamber segmentation in CT images have been developed [27–29]. Higgins et al. developed a semi-automatic method that relies on some manual slice-by-slice editing to guide automatic grayscale and shape-based processing; their method shows good LV chamber volume correlation with manual analyses [27]. A popular LV chamber segmentation approach is to use deformable 2D contours or 3D surfaces attracted to the gradient maxima. Staib and Duncan used a 3D surface model of the LV to segment the chamber from CT data [28]. Their method is initialized by configuring the model to an

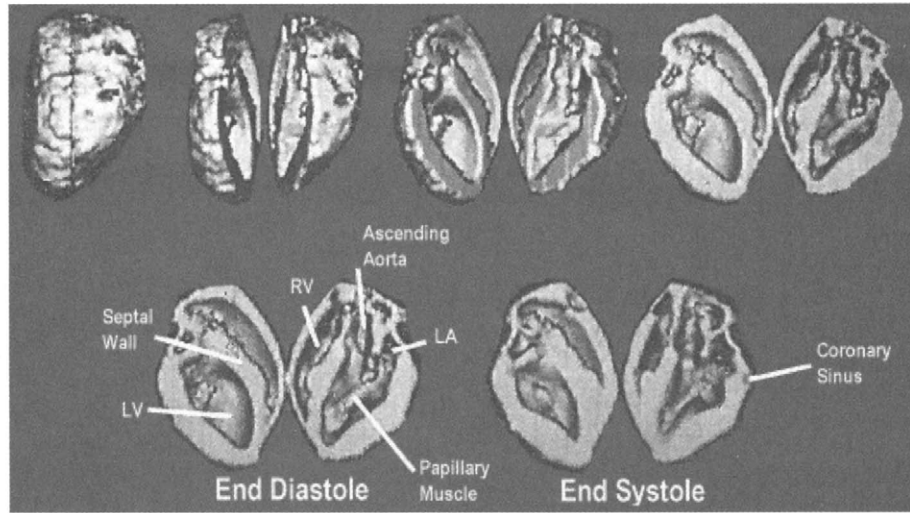


FIGURE 12 Virtual endoscopic views of a heart. Top row of figure shows computer-generated “dissection” of the 3D heart volume. Bottom row has partially labeled heart anatomy. LA, left atrium; RV, right ventricle. From [31].

average chamber shape, and then deforming the model based on local gradient information. Related work from the same group uses a 3D shape model and combined grayscale region statistics with edge information for robust LV chamber segmentation [29].

Figure 12 shows surface-rendered interior views—i.e., virtual endoscopic views—of a canine heart from a 3D DSR data set. This figure was created by manually tracing region boundaries on the image, and then shading surface pixels based on the angle between the viewing position and the local surface normal. The image clearly shows the four-chambered heart, the valves, and the myocardium.

Some work has been done toward true four-dimensional (4D) processing of cardiac image data. In [30] the user first defines a series of graphically defined image-segmentation cues, using a graphics-based computer system. Next, a set of image-processing operations, drawing upon mathematic morphology, 3D topological analysis, and image segmentation is derived for the segmentation problem using the cues. After this set of operations is run automatically on the 4D image, all timepoints of the sequence are segmented. Figure 13 shows how the semi-automatic approach yields better defined results more quickly than standard manual slice editing.

3.1.3 Echocardiography

Echocardiography uses ultrasound energy to image the heart [21]. The ultrasound energy (in the form of either a longitudinal or transverse wave) is applied to the body through a transducer with piezo-electric transmit and receive ultrasound crystals. As the ultrasound wave propagates through the body, some energy is reflected when the wavefront encounters a change in acoustic impedance (due to a change in tissue type). The ultrasound receiver detects this return signal and uses it to form the image. Because ultrasound imaging does

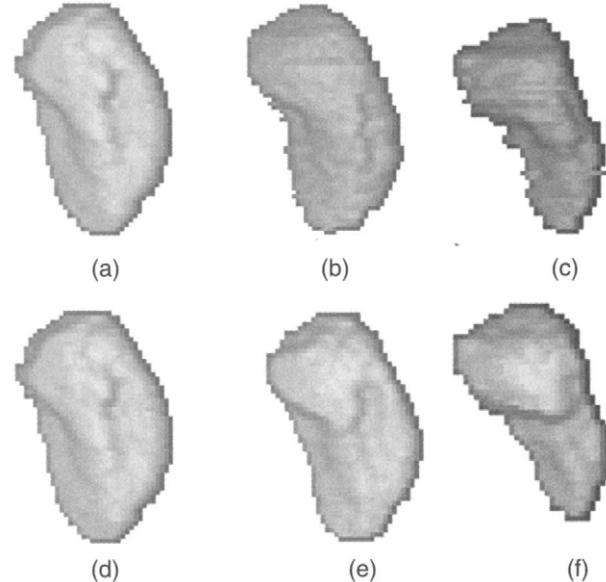


FIGURE 13 3D surface-rendered views of the segmented LV chamber. A sequence of 16 3D DSR cardiac images were used for the test, where 16 images span one heart cycle from end diastole (time point 1) to end systole (time point 8) to end diastole of the next cycle (time point 16). Each time point was acquired 33 ms apart. (a–c): Manually segmented results for timepoints 1, 3, and 8. (d–f): Results for timepoints 1, 3, and 8 from semi-automatic 4D segmentation. From [30].

not use ionizing radiation to construct the image, ultrasound exams can be repeated many times without worries of cumulative radiation exposure. Ultrasound systems are often inexpensive, portable, and easy to operate, and as a result, exams are often performed at the bedside or in an examination room.

Common cardiac ultrasound imaging applications use energy in the range of 1 to about 25 MHz, although higher frequencies may be used for IVUS imaging. Most clinical ultrasound scanners can acquire B-mode (brightness) images,

M-mode (motion) images, and doppler (velocity) images. In B-mode imaging, a 2D sector scan is used to create an image where pixel brightness in the image is proportional to the strength of the received echo signal. Several B-mode images may be obtained at different orientations to approximate volume imaging. In M-mode imaging, a 2D image is formed where one image axis is distance from the transducer and the other axis is time. As with B-mode, pixel intensities in the M-mode image are proportional to the strength of the received echo signal. M-mode images can be used to track myocardial wall and valve motion. Doppler imaging uses the frequency shift in the received signal to estimate the

velocity of ultrasound scatterers. Doppler imaging can be used to measure wall and valve motion, and to assess blood flow through the arteries and heart. New 3D ultrasound scanners have been introduced. These scanners use an electronically steered 2D phased array transducer to acquire a volumetric data set. The 3D ultrasound scanners can acquire data sets at near video rates (10–20 3D images per second). Figure 14 shows several views of a 3D ultrasound data set, after image segmentation and surface modeling.

Much work in cardiac ultrasound image processing has been focused on edge detection in 2D B-mode images to eliminate the need for manual tracing of the endocardial

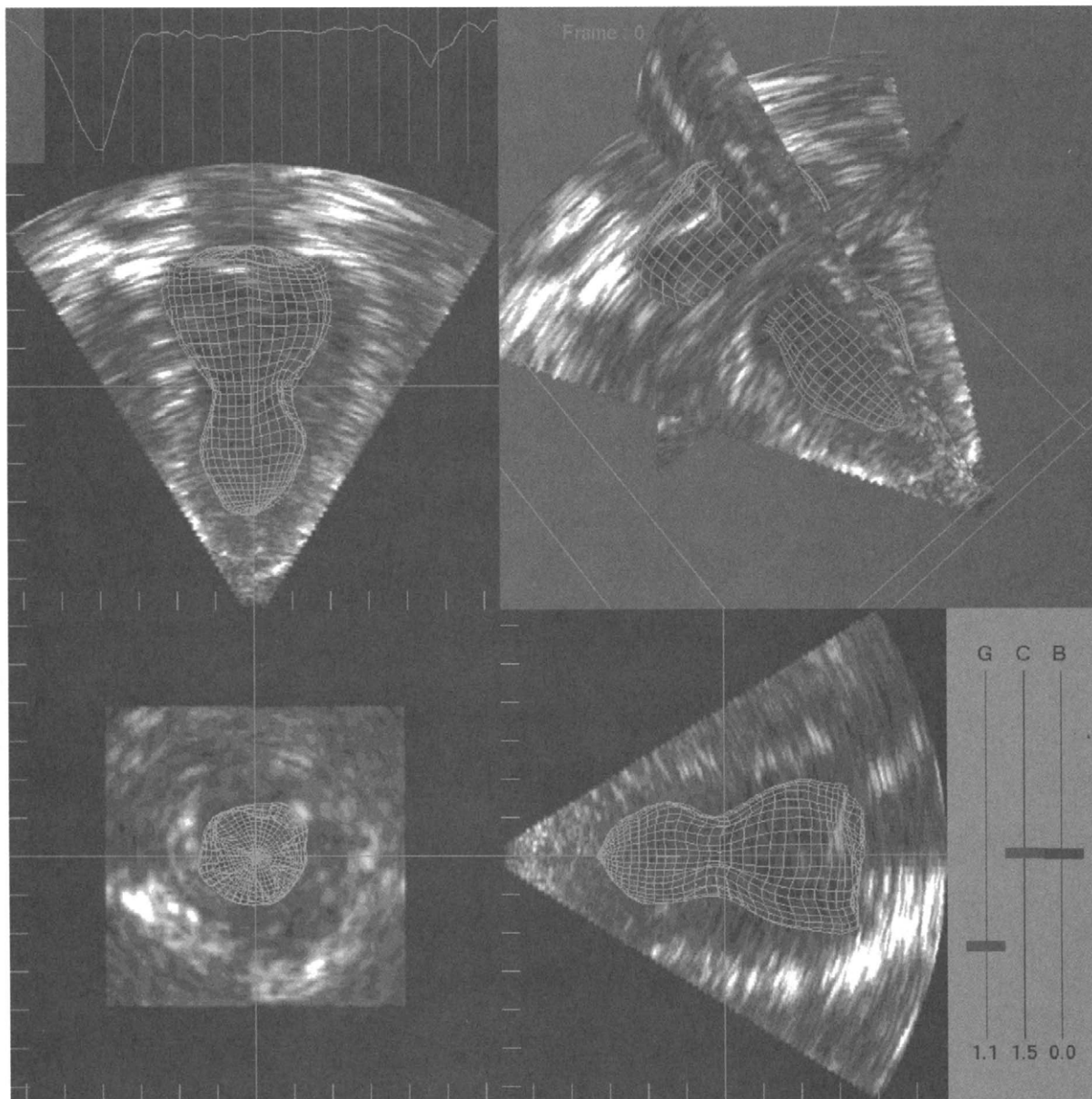


FIGURE 14 3D ultrasound image of human heart. Figure shows image analysis and display system with four different views of the image data and surface reconstruction overlay based on image segmentation results. (Figure courtesy of Dr. Edwin L. Dove, University of Iowa.) (See color insert.)

and epicardial borders [2]. The first step in the processing is often some preprocessing filtering, such as a median filter, to reduce noise in the image. Preprocessing is followed by an edge detection step, with a 2D operator such as the Sobel or Prewitt edge detection mask, to identify strong edges in the image. Finally, the strong edges are linked together to form a closed boundary around the ventricle. This automatic 2D processing shows good correlation with contours manually traced by a human [2]. After identifying the ventricle on each slice of a 3D stack of B-mode images, a 3D surface can be reconstructed and visualized.

Deformable contour models have also been successfully applied to the segmentation of LV chamber borders in echo cardiographic images [32]. Another approach for LV chamber detection in echocardiography has focused on using optimization algorithms to identify likely border pixels. For these approaches, the image is processed with an edge detection operator to compute the edge strength at each pixel. The edge strength at each pixel is converted to a cost value, where the cost assigned to a pixel is inversely proportional to the likelihood that the pixel lies on the true LV border. Graph searching or dynamic programming is used to find a minimum-cost path through the image, corresponding to the most likely location of the LV chamber border. More sophisticated approaches can incorporate *a priori* region shape, texture, and deformation information into an anatomic model that can be used to guide image segmentation [33].

3.1.4 Magnetic Resonance Imaging

MR imaging is being increasingly used for studying the heart and cardiovascular system [22], and new, faster MR scanners are being developed specifically for this purpose. Because of differences in their magnetic susceptibility, there is natural contrast between the myocardium and the blood pool. MR contrast agents are now available to further enhance cardiac and vascular imaging. Figure 7 shows an image acquired of the right coronary artery; the same image, however, depicts the cardiac chambers and myocardium. Many of the same image analysis techniques used in echocardiography and CT are applicable to cardiac MR image analysis; for example, 2D and 3D border detection algorithms based on optimal graph searches have been applied to LV chamber segmentation in MR images [34]. New methods, based on statistical models of cardiac shape and deformation, have been successfully applied to 2D, 2D plus time, and 3D cardiac MR data [33, 35].

3.2 Myocardial Wall Motion and Wall Mechanics

If a time series of images showing the heart chamber motion is available, information such as regional chamber wall velocity, myocardial thickening, and muscle strain can be computed. This analysis requires that the LV boundary be determined

at each time point in the image sequence. After the LV boundary has been determined, motion estimation requires that the point-to-point correspondences be determined between the LV border pixels in images acquired at different times. For this difficult problem, algorithms based on optical flow [36] and shape-constrained minimum-energy deformations [37] have been successfully applied to CT and echo cardiographic images.

One of the most important recent advances in cardiac imaging has been the development of non-invasive techniques to “tag” specific regions of tissue within the body [38, 39]. These tagging techniques, all based on MR imaging, use a pre-saturation RF pulse to temporarily change the magnetic characteristics of the nuclei in the tagged region just prior to image acquisition. The tagged region will have a greatly attenuated NMR response signal compared to the untagged tissue. Because the tags are associated with a particular spatial region of tissue, if the tissue moves, the tags move as well. Thus, by acquiring a sequence of images across time, the local displacement of the tissue can be determined by tracking the tags. One common cardiac tagging technique is called spatial modulation of magnetization (SPAMM) [38, 39]. SPAMM tags are often applied as grid lines, as illustrated in Fig. 15.

The two major image analysis problems in SPAMM imaging are the detection of the tag points and tracking and registering the tag points as the tissue deforms. Young et al. used a mesh of snakes to detect the tag lines in SPAMM images and tracked the tag lines and their intersection points between images [40]. The deformation information in [40] was used to drive a finite element model of the myocardium. Denney and Prince used an information theoretic framework to estimate the 3D motion of the myocardium from a stochastic model of heart motion that incorporated *a priori* information about the heart dynamics and smoothness constraints [41]. Park et al. analyzed the dynamic LV chamber using 3D deformable models. The models were parameterized by functions representing the local LV surface shape and deformation parameters. Their approach gave estimates of LV radial contraction, longitudinal contraction, and twisting. Amini used B-spline snakes to detect the tag lines. The B-splines were part of a thin-plate myocardial model that could be used to estimate myocardial deformation (compression, torsion, etc.) and strain at sample points between the tag line intersections [42]. Figure 16 shows a 3D myocardial wall model computed by tracking SPAMM tag line motion during the heart cycle.

Papademetris et al. describe a technique for modality-independent analysis of LV chamber deformation [43]. Their method is driven by segmented LV chamber regions that are tracked across time using a shape-tracking approach combined with a linear-elastic model of the heart muscle. Since corresponding points are computed as part of the analysis, SPAMM is unnecessary, and the method is applicable to MR, CT, and other cardiac imaging modalities. After

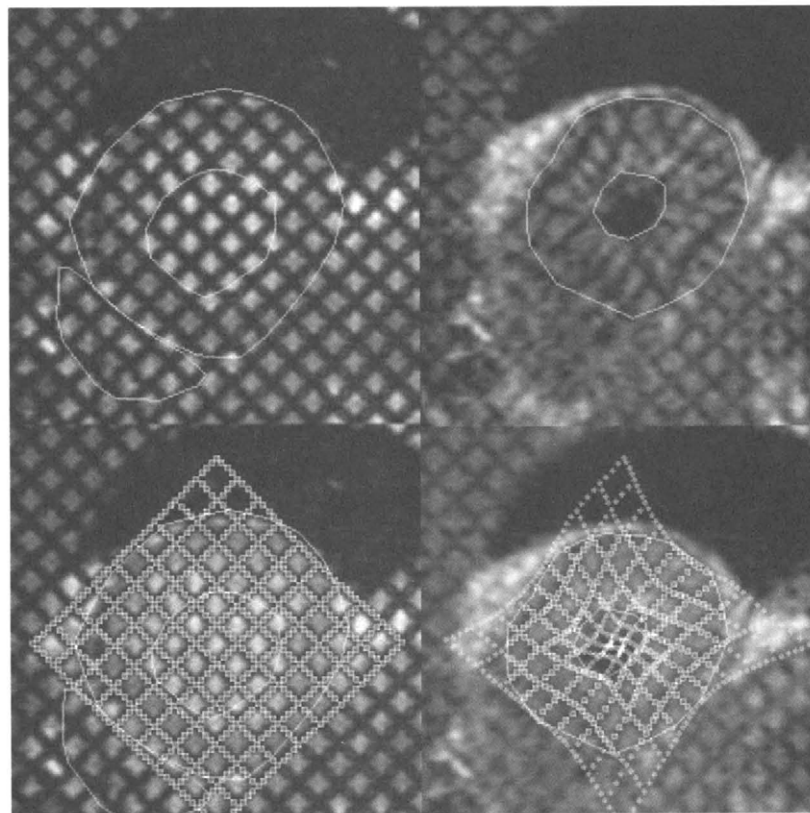


FIGURE 15 MR image showing SPAMM tag lines. Top left: Initial tag line configuration. Manually traced contours show chamber borders. Top right: After heart has changed shape. Tag lines have deformed to provide an indication of myocardial deformation. Bottom left and right: detected tag lines. From [40].

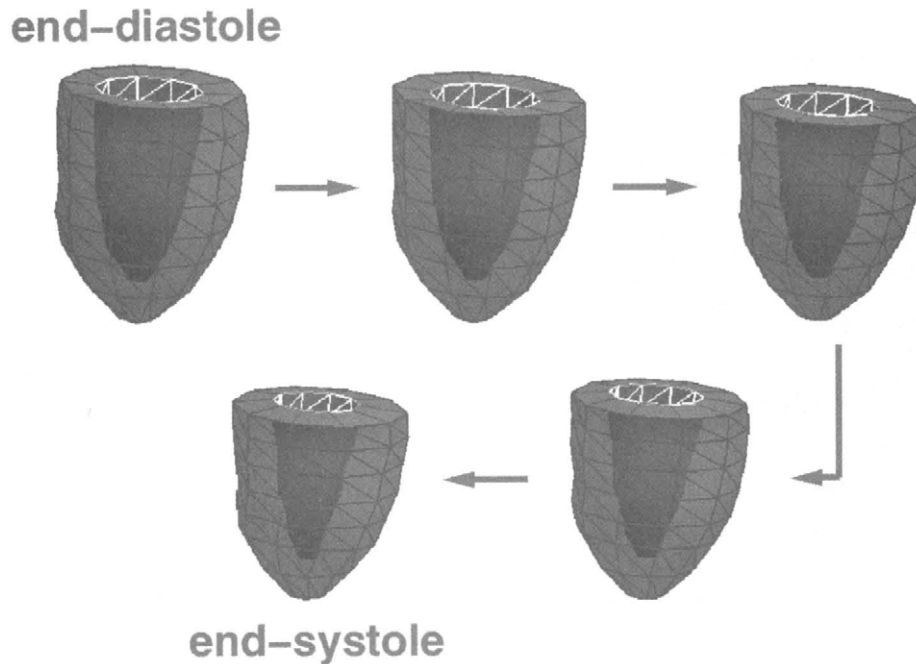


FIGURE 16 3D myocardial wall model derived from deformable surface tracking SPAMM tag lines. Model shows inner and outer borders of myocardium. Figure shows the evolution of myocardial wall and LV chamber shape from end diastole to end systole. (Figure courtesy of Dr. Jinah Park, University of Pennsylvania.) (See color insert.)

processing, biomechanical parameters, including local heart muscle strains, are computed.

4 Myocardial Blood Flow (Perfusion)

Coronary angiography can be used to evaluate the structure of the coronary artery tree and to detect and quantify arterial stenoses. However, the precise linkage between coronary artery stenoses and blood flow (perfusion) to the myocardium is unclear [44]. Angiographic imaging is also limited by the spatial resolution of the imaging system. The largest coronary arteries are easily identified and analyzed. But, the vast network of smaller arteries that actually deliver blood to the myocardium remain mostly undetectable on the images. In this section we describe imaging modalities capable of directly assessing myocardial perfusion. The primary use of these techniques is to detect perfusion flow deficits beyond an arterial stenosis.

Positron emission tomography (PET) and single photon emission computed tomography (SPECT) both use intravenously injected radiopharmaceuticals to track the flow of blood into the myocardial tissue. An image is formed where the pixels in the image represent the spatial distribution of the radiopharmaceutical. An example SPECT myocardial perfusion image is shown in Fig. 17.

Both echocardiographic and MR imaging can also be used to assess myocardial blood flow. In both cases, a contrast agent is used to increase the signal response from the blood. In echocardiography, small microbubbles (on the order of 5 microns in diameter) are injected into the bloodstream [44]. Bubbles this small can move through the pulmonary circulation and travel to the myocardium through the coronary arteries. The large difference in acoustic impedance between

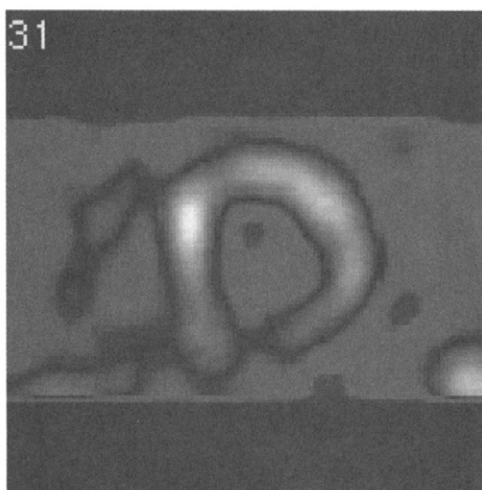


FIGURE 17 SPECT myocardial perfusion analysis using injected thallium-201 tracer. Image shows cross-sectional view of myocardium (LV chamber is the cavity at center of the image), with pixel intensity proportional to myocardial blood flow distribution. (Image courtesy of Dr. Richard Hichwa, PET Imaging Center, University of Iowa.) (See color insert.)

the blood and the bubbles results in a dramatic increase in the echo signal back from the perfused myocardium. For MR imaging, new injectable MR contrast agents have been developed to serve a similar purpose.

An interesting image processing challenge related to perfusion imaging is the problem of registering the functional (blood flow) images to structural (anatomic) images obtained using other modalities [45]. This structure-function matching typically uses anatomic landmarks and/or external fiducial markers to find an affine transformation to align the two image data sets. The results can be visualized by combining the images so that a thresholded blood flow image is overlaid in pseudo-color on the anatomic image.

5 Electrocardiography

The constant muscular contractions of the heart during the cardiac cycle are triggered by regular electrical impulses originating from the heart's sino-atrial node (the heart's "pacemaker"). These impulses conduct throughout the heart, causing the movement of the heart's muscle. Certain diseases can produce irregularities in this activity; if it is sufficiently interrupted, it can cause death. This electrical activity can be recorded and monitored as an electrocardiogram (ECG).

Through the techniques of electrocardiographic imaging, ECG data can be mapped into a 2D or 3D image [46]. These so-called body-surface potential maps are constructed by simultaneously recording and assembling a series of ECGs. Such image data can be used to visualize and evaluate various disease states, such as myocardial ischemia, where the blood flow is reduced to a portion of the myocardium. Angiographic and CT imaging cannot provide such data. Body-surface potential maps also permit the study of ventricular fibrillation, a condition when the heart is excited by chaotic—and potentially lethal—electrical impulses.

Standard analytic methods from electromagnetics, such as the application of Green's theorem to compute the electric field distributions within the heart volume, are applied to evaluate such image data. Figure 18 gives an example. Recent work has combined sophisticated computer-graphics techniques and stereoscopic imaging to enable better localization and analysis of ECG data [47].

6 Summary and View of the Future

Cardiovascular imaging is a major focus of modern healthcare. Many modalities are available for cardiac imaging. The image processing challenges include the development of robust image segmentation algorithms to minimize routine manual image analysis, methods for accurate measurement of clinically-relevant parameters, techniques for visualizing and modeling these complex multidimensional data sets,

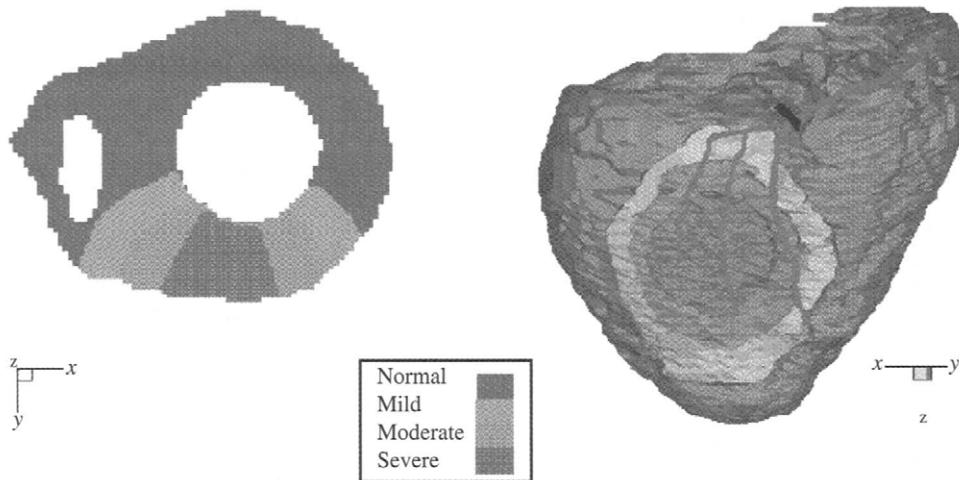


FIGURE 18 Example of a body-surface potential map. The left side shows a mapping for a 2D slice through the heart; the cavities correspond to the ventricles. The right side shows a 3D surface-rendered view of the same map. The color-coding indicates the degree of myocardial ischemia (reduction in blood flow). The red lines on the 3D view indicate a stenosed arterial region that brought about the ischemia. From [46].

and tools for using the image information to guide surgical interventions.

As technology continues to advance, scanner hardware and imaging software will continue to improve as well. Faster scanners with higher-resolution detectors will improve image quality. Researchers will continue the move toward scanning systems that provide true 3D and 4D image acquisition; see [48, 49] for recent special issues on this topic. From the image processing perspective, there will be a need to quickly process large multidimensional data sets, and to provide easy-to-use tools to inspect and visualize the results.

The interest in cardiovascular imaging is evidenced by the large number of journals, conferences, and workshops devoted to this area of research. From the engineering perspective, the *IEEE Transactions on Medical Imaging*, *IEEE Transactions on Biomedical Engineering*, *IEEE Transactions on Image Processing*, and the *IEEE Engineering in Medicine and Biology Society Magazine* carry articles related to cardiac imaging. Conferences such as *Computers in Cardiology*, the *IEEE International Conference on Image Processing*, the *IEEE International Symposium on Biomedical Imaging*, the *SPIE Conference on Medical Imaging*, and the *IEEE Engineering in Medicine and Biology Annual Meeting* are good sources for the most recent advances in cardiac imaging and image processing.

Acknowledgments

The following people have contributed figures and comments to this chapter: Drs. Edwin Dove, Richard Hichwa, Eric Hoffman, Charles Rossen, Milan Sonka, Daniel Thedens, and Andreas Wahle, of the University of Iowa, Dr. David

McPherson of Northwestern University, and Dr. Jinah Park of the University of Pennsylvania.

References

- [1] M. L. Marcus, H. R. Schelbert, D. J. Skorton, and G. L. Wolf, *Cardiac Imaging*. Philadelphia: W. B. Saunders, 1991.
- [2] S. M. Collins and D. J. Skorton, eds., *Cardiac Imaging and Image Processing*. New York: McGraw-Hill, 1986.
- [3] G. M. Pohost et al., ed., *Imaging in Cardiovascular Disease*. Philadelphia: Lippincott, Williams, and Wilkins, 2000.
- [4] A. Wahle, E. Wellnhofer, I. Mugaragu, H. U. Sauer, H. Oswald, and E. Fleck, "Assessment of diffuse coronary artery disease by quantitative analysis of coronary morphology based upon 3D reconstruction from biplane angiograms," *IEEE Trans. Medical Imaging*, 14, 2, 230–241, June 1995.
- [5] K. Kitamura, J. B. Tobis, and J. Sklansky, "Estimating the 3D skeletons and transverse areas of coronary arteries from biplane angiograms," *IEEE Trans. Medical Imaging*, 7, 3, 173–187, Sept. 1988.
- [6] T. N. Pappas and J. S. Lim, "A new method for estimation of coronary artery dimensions in angiograms," *IEEE Trans. Acoustics, Speech, and Signal Proc.*, 36, 9, 1501–1513, Sept. 1988.
- [7] S. R. Fleagle, M. R. Johnson, C. J. Wilbricht, D. J. Skorton, R. F. Wilson, C. W. White, and M. L. Marcus, "Automated analysis of coronary arterial morphology in cineangiograms: Geometric and physiologic validation in humans," *IEEE Trans. Medical Imaging*, 8, 4, 387–400, Dec. 1989.
- [8] Y. Sun, R. J. Lucariello, and S. A. Chiaramida, "Directional low-pass filtering for improved accuracy and reproducibility of stenosis quantification in coronary arteriograms," *IEEE Trans. Medical Imaging*, 14, 2, 242–248, June 1995.
- [9] A. K. Klein, F. Lee, and A. A. Amini, "Quantitative coronary angiography with deformable spline models," *IEEE Trans. Medical Imaging*, 16, 5, 468–482, Oct. 1997.

- [10] D. L. Parker, D. L. Pope, R. van Bree, and H. W. Marshall, "Three-dimensional reconstruction of moving arterial beds from digital subtraction angiography," *Comput. Biomed. Res.*, 20, 2, 166–185, Apr. 1987.
- [11] I. Liu and Y. Sun, "Fully automated reconstruction of three-dimensional vascular tree structures from two orthogonal views using computational algorithms and production rules," *Opt. Engin.*, 31, 10, 2197–2207, Oct. 1992.
- [12] M. Block, Y. H. Liu, D. Harris, R. A. Robb, and E. L. Ritman, "Quantitative analysis of a vascular tree model with the dynamic spatial reconstructor," *J. Comp. Assist. Tomogr.*, 8, 2, 390–400, June 1984.
- [13] W. E. Higgins, R. A. Karwoski, W. J. T. Spyra, and E. L. Ritman, "System for analyzing true three-dimensional angiograms," *IEEE Trans. Medical Imaging*, 15, 3, 377–385, June 1996.
- [14] C. R. Becker, U. J. Schoepf, and M. F. Reiser, "Methods for quantification of coronary artery calcifications with electron beam and conventional CT and pushing the spiral CT envelope: New cardiac applications," *Int. J. Cardiovascular Imaging*, 17, 3, 203–211, June 2001.
- [15] W. Kalender, *Computed Tomography: Fundamentals, System Technology, Image Quality, Applications*. Munich: Publicis MCD Verlag, 2000.
- [16] G. Wang, C. Crawford, and W. Kalender, eds., "Special issue on multirow detector and cone-beam spiral/helical CT," *IEEE Trans. Medical Imaging*, 19, 9, September 2000.
- [17] H. Jin, K. Ham, J. Chan, L. Butler, R. Kurtz, S. Thiam, J. Robinson, R. Agbaria, I. Warner, and R. Tracy, "High resolution three-dimensional visualization and characterization of coronary atherosclerosis in vitro by synchrotron radiation X-ray microtomography and highly localized X-ray diffraction," *Physics in Medicine and Biology*, 47, 21, 4345–4356, December 2002.
- [18] S. Y. Wan, E. L. Ritman, and W. E. Higgins, "Multi-generational analysis and visualization of the vascular tree in 3D micro-CT images," *Computers in Biology and Medicine*, 32, 2, 55–71, Feb. 2002.
- [19] K. C. Yu, E. L. Ritman, and W. E. Higgins, "Graphical tools for improved definition of 3D arterial trees," in *SPIE Medical Imaging 2004: Physiology, Function, and Structure -- Methods, Systems, and Applications*, 5369, 485–495, A. Amini and A. Manduca, Eds., 2004.
- [20] M. Kretowski, Y. Rolland, J. Bezy-Wendling, and J. L. Coatrieux, "Physiologically based modelling of 3D vascular networks and CT scan angiography," *IEEE Trans. Medical Imaging*, 22, 3, 248–257, February 2003.
- [21] K. K. Shung, M. B. Smith, and B. M. W. Tsui, *Principles of Medical Imaging*. San Diego: Academic Press, 1992.
- [22] J. P. Earls, V. B. Ho, T. K. Foo, E. Castillo, and S. D. Flamm, "Cardiac MRI: Recent progress and continued challenges," *J. Magnetic Resonance Imaging*, 16, 2, 111–127, August 2002.
- [23] A. Wahle, "Quantification of coronary hemodynamics and plaque morphology using x-ray angiography and intravascular ultrasound," in *Computer Assisted Radiology and Surgery (CARS 2004)*, H. Lemke, M. Vannier, K. Inamura, A. Farman, K. Doi, and J. Reiber, eds., 1268, 1035–1039, 2004.
- [24] A. Wahle, M. E. Olszewski, and M. Sonka, "Interactive virtual endoscopy in coronary arteries based on multi-modality fusion," *IEEE Trans. Medical Imaging*, 2004, 139–1403, 23, 11, Nov. 2004.
- [25] P. Rogalla, J. Terwisscha van Scheltinga, and B. Hamm, eds., *Virtual Endoscopy and Related 3D Techniques*. Berlin: Springer, 2000.
- [26] K. B. Chandran, *Cardiovascular Biomechanics*. New York: New York University Press, 1992.
- [27] W. E. Higgins, N. Chung, and E. L. Ritman, "Extraction of the left-ventricular chamber from 3D CT images of the heart," *IEEE Trans. Medical Imaging*, 9, 4, 384–395, Dec. 1990.
- [28] L. H. Staib and J. S. Duncan, "Model-based deformable surface finding for medical images," *IEEE Trans. Medical Imaging*, 15, 5, 720–731, Oct. 1996.
- [29] A. Chakraborty, L. H. Staib, and J. S. Duncan, "Deformable boundary finding in medical images by integrating gradient and region information," *IEEE Trans. Medical Imaging*, 15, 6, 859–870, Dec. 1996.
- [30] J. M. Reinhardt, A. J. Wang, T. P. Weldon, and W. E. Higgins, "Cue-based segmentation of 4D cardiac image sequences," *Computer Vision and Image Understanding*, 77, 251–262, Feb. 2000.
- [31] J. K. Udupa and G. T. Herman, eds., *3D Imaging in Medicine*. Boca Raton, FL: CRC Press, 1991.
- [32] V. Chalana, D. T. Linker, D. R. Haynor, and Y. Kim, "A multiple active contour model for cardiac boundary detection on echocardiographic sequences," *IEEE Trans. Medical Imaging*, 15, 3, 290–298, June 1996.
- [33] S. C. Mitchell, B. P. F. Lelieveldt, R. J. van der Geest, H. G. Bosch, J. H. C. Reiber, and M. Sonka, "Multistage hybrid active appearance model matching: Segmentation of left and right ventricles in cardiac MR images," *IEEE Trans. Medical Imaging*, 20, 5, 415–423, May 2001.
- [34] D. R. Thedens, D. J. Skorton, and S. R. Fleagle, "Methods of graph searching for border detection in image sequences with applications to cardiac magnetic resonance imaging," *IEEE Trans. Medical Imaging*, 14, 1, 42–55, March 1995.
- [35] S. C. Mitchell, J. G. Bosch, B. P. F. Lelieveldt, R. J. van der Geest, J. H. C. Reiber, and M. Sonka, "3D active appearance models: Segmentation of cardiac MR and ultrasound images," *IEEE Trans. Medical Imaging*, 21, 9, 1167–1178, September 2002.
- [36] S. Song and R. Leahy, "Computation of 3D velocity fields from 3D cine CT images," *IEEE Trans. Medical Imaging*, 10, 3, 295–306, Sept. 1991.
- [37] J. C. McEachen, II and J. S. Duncan, "Shape-based tracking of left ventricular wall motion," *IEEE Trans. Medical Imaging*, 16, 3, 270–283, June 1997.
- [38] E. A. Zerhouni, D. M. Parish, W. J. Rogers, A. Yang, and E. P. Shapiro, "Human heart: Tagging with MR imaging—A method for noninvasive assessment of myocardial motion," *Radiology*, 169, 59–63, 1988.
- [39] L. Axel and L. Dougherty, "Heart wall motion: Improved method of spatial modulation of magnetization for MR imaging," *Radiology*, 172, 2, 349–350, Aug. 1989.

- [40] A. A. Young, D. L. Kraitchman, L. Dougherty, and L. Axel, "Tracking and finite element analysis of stripe deformation in magnetic resonance tagging," *IEEE Trans. Medical Imaging*, 14, 3, 413–421, Sept. 1995.
- [41] T. S. Denney and J. L. Prince, "Reconstruction of 3D left ventricular motion from planar tagged cardiac MR images: An estimation theoretic approach," *IEEE Trans. Medical Imaging*, 14, 4, 625–635, December 1995.
- [42] A. A. Amini, Y. Chen, R. W. Curwen, and J. Sun, "Coupled B-snake grids and constrained thin-plate splines for the analysis of 2D tissue deformations from tagged MRI," *IEEE Trans. Medical Imaging*, 17, 3, 344–356, June 1998.
- [43] X. Papademetris, A. Sinusas, D. Dione, R. T. Constable, and J. Duncan, "Estimation of 3D left ventricular deformation from medical images using biomechanical models," *IEEE Trans. Medical Imaging*, 21, 7, 786–800, July 2002.
- [44] J. H. C. Reiber and E. E. van der Wall, eds., *Cardiovascular Imaging*. Dordrecht: Kluwer Academic, 1996.
- [45] M. C. Gilardi, G. Rizzo, A. Savi, and F. Fazio, "Registration of multi-modality biomedical images of the heart," *Quarterly J. of Nuclear Medicine*, 40, 1, 142–150, Mar. 1996.
- [46] R. M. Gulrajani, "The forward and inverse problems of electrocardiography," *IEEE Engin. in Med. & Bio. Magazine*, 17, 5, 84–101, Sept.–Oct. 1998.
- [47] R. Ghanem, C. Ramanathan, P. Jia, and Y. Rudy, "Heart-surface reconstruction and ECG electrodes localization using fluoroscopy, epipolar geometry and stereovision: application to noninvasive imaging of cardiac electrical activity," *IEEE Trans. Medical Imaging*, 22, 10, 1307–1318, October 2003.
- [48] A. Frangi, D. Rueckert, and J. Duncan, eds., "Special issue on three-dimensional cardiovascular image analysis," *IEEE Trans. Medical Imaging*, 21, 9, September 2002.
- [49] A. Frangi, A. Amini, and E. Bullitt, eds., "Special issue on vascular imaging," *IEEE Trans. Medical Imaging*, 24, 3, March 2005.

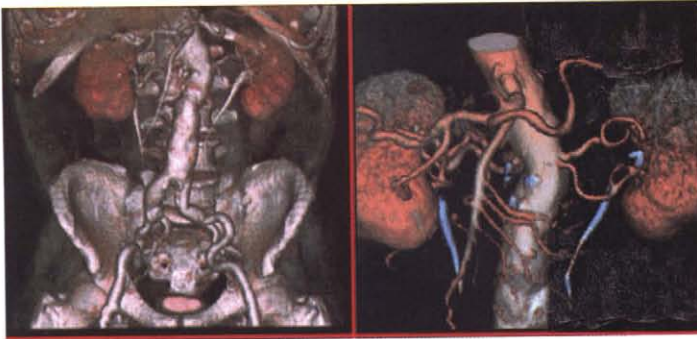
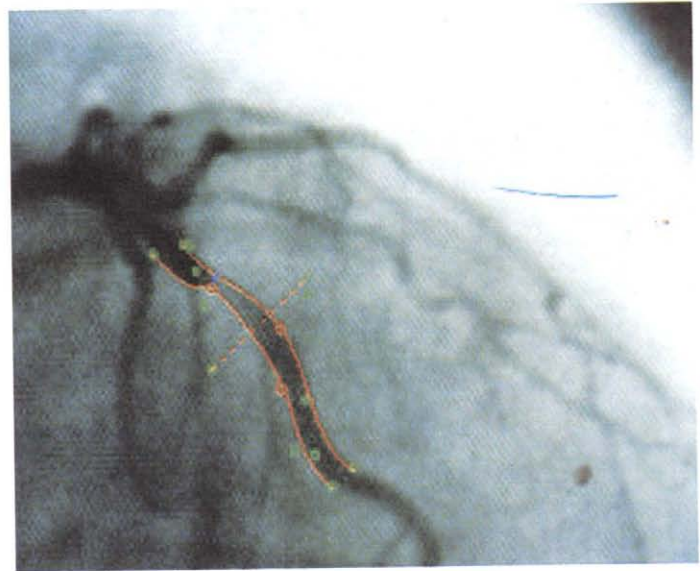


FIGURE 10.2.5 Volume rendering from a sequence of x-ray CT images showing the abdominal cavity and kidneys (CT images courtesy of G. E. Medical Systems).

FIGURE 10.3.3 Result of active-contour analysis applied to a selected artery in a typical 2-D angiogram. The green points are the manually identified control points. The red lines are the computed vessel wall borders. From [9].

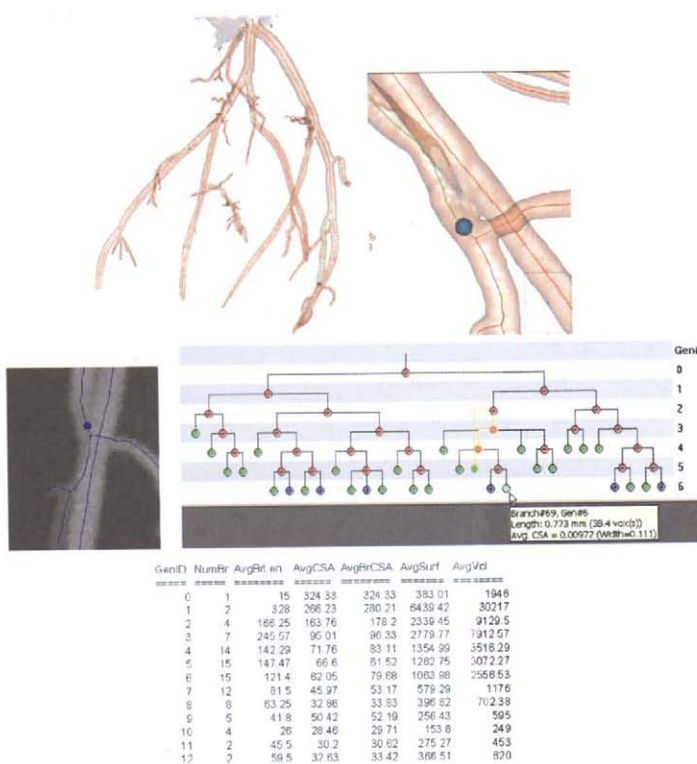


FIGURE 10.3.6 Composite view of system for analyzing a 3-D arterial tree [19]. (a) Surface-rendered version of the extracted 3-D arterial tree; a tree defect is marked by a ball; in all views the lines denote the tree central axes. (b) Local surface rendering of tree about the selected defect. (c) Local depth-weighted slab of original 3-D gray-scale data about defect. (d) Quantitative description of final tree [18]. (e) Graph of corrected tree; nodes signify branch points; circles with plusses signifying graph nodes that can be expanded further; a node (branch) is selected to show its local quantitative description.

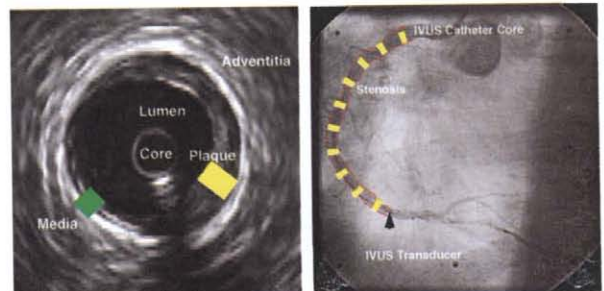


FIGURE 10.3.8 Angiographic and IVUS views of the coronary arteries. Right view is a 2-D angiogram; arrow indicates location of the IVUS transducer. Left view shows corresponding cross-sectional IVUS frame of the arterial lumen. (Figure courtesy of Dr. Andreas Wahle, University of Iowa.)

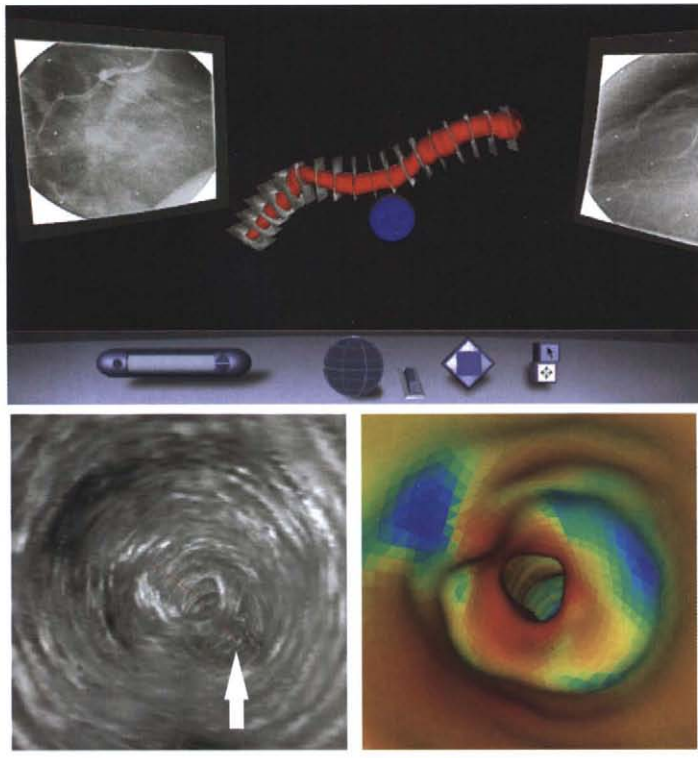


FIGURE 10.3.9 Views from a VRML-based angiographic-IVUS fusion system. Top shows VRML display and navigation system. Bottom view depicts a 3-D virtual angioscopic display of artery surface using the original IVUS data (left) and with color-coded shear stress mapped onto the reconstructed surface (right). From [24].

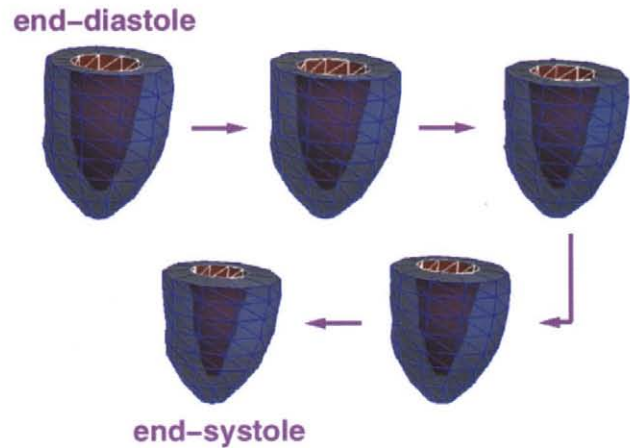


FIGURE 10.3.16 3-D myocardial wall model derived from deformable surface tracking SPAMM tag lines. Model shows inner and outer borders of myocardium. Figure shows the evolution of myocardial wall and LV chamber shape from end diastole to end systole. (Figure courtesy of Dr. Jinah Park, University of Pennsylvania.)

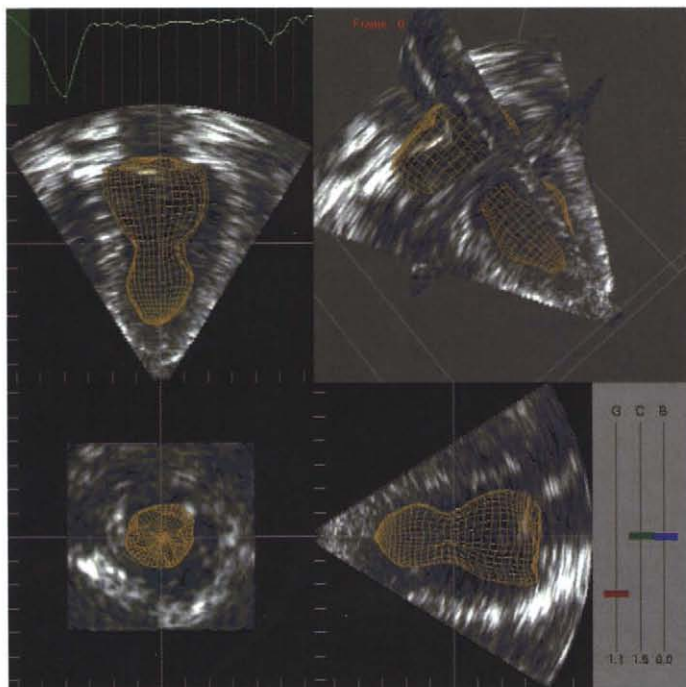


FIGURE 10.3.14 3-D ultrasound image of human heart. Figure shows image analysis and display system with four different views of the image data and surface reconstruction overlay based on image segmentation results. (Figure courtesy of Dr. Edwin L. Dove, University of Iowa.)



FIGURE 10.3.17 SPECT myocardial perfusion analysis using injected thallium-201 tracer. Image shows cross-sectional view of myocardium (LV chamber is the cavity at center of the image), with pixel intensity proportional to myocardial blood flow distribution. (Image courtesy of Dr. Richard Hichwa, PET Imaging Center, University of Iowa.)